Comparison of Very High Cycle Fatigue Properties of 18CrNiMo7-6 Steel after Carburizing and Pseudo-carburizing

Peifeng Cheng (ID), Yunkun Li, Wenchao Yu, Shaopeng Yang, Fangzhong Hu, Jie Shi, Maoqiu Wang, and Li Li

The very high cycle fatigue (VHCF) properties of case hardening steel 18CrNiMo7-6 after carburizing and pseudo-carburizing have been investigated by means of ultrasonic fatigue tests. Results showed that the pseudo-carburized specimens with the hardness of 442 HV did not show VHCF fracture, and fatigue fracture did not occur even after 10^9 cycles when the applied stress amplitude was lower than the high cycle fatigue limit of 650 MPa obtained at 10^7 cycles. When carburized thoroughly with the hardness of 700 HV, the experimental steel showed VHCF phenomenon, and it might fracture even at nearly 10^9 cycles when the stress amplitude was about 600 MPa. Observations of the fracture surfaces of the fatigue specimens showed that after carburizing, the fatigue crack initiation sites changed from martensite matrix to nonmetallic inclusions, forming granular bright facet (GBF) and fish-eye before final abrupt fracture. The stress intensity factor at GBF area, which was calculated to be 3.5 MPa m$^{1/2}$, could be used as a critical value for VHCF fracture for the carburized specimens of the experimental steel. The VHCF fracture of the carburized specimens of the experimental steel could be related to the high hardness and large amount of retained austenite as a result of carburizing.

1. Introduction

Very high cycle fatigue (VHCF) properties of high-strength steels such as bearing steel JIS SUJ2, spring steel JIS SUP7 and bolt steel JIS SCM440 have been extensively investigated in recent years (Ref 1-4). It is known that high-strength steels may fracture at a stress below the classical fatigue limit, which is determined in the high cycle fatigue regime of 10^7 cycles, when they are stressed in the VHCF regime (Ref 5, 6). Thus, the fatigue limits under the life of 10^9 cycles, which can be readily measured by ultrasonic fatigue tests (Ref 7), are always used to characterize the VHCF properties of high-strength steels. From the engineering point of view, data of VHCF properties of high-strength steels are needed to ensure their service safety in a long period.

Case hardening steels are widely used for gears and shafts, of which VHCF life is needed to be considered in some cases such as components in gear box for high-speed train. Actually, the very early study of VHCF phenomenon was carried out by means of rotating bending fatigue tests for case carburized steel by Naito et al. and Nehila et al. (Ref 8, 9). It was found that the carburized specimens fractured at a cycle of over 10^7 cycles, which was inconsistent with the traditional theory of fatigue limit. Under rotating bending fatigue tests, it was the surface where stress amplitude was the highest and thus the fracture would always initiate in the near-surface carburized case. Ultrasonic fatigue tests are commonly used for VHCF investigation due to the high frequency and efficiency, however, it is not easy to be carried out for carburized specimens, because it is unknown where the fatigue crack might initiate under a uniform cross-sectional stress amplitude due to the gradient in-depth distributions of carbon content, microstructure and hardness in the carburized specimens (Ref 10-12). Sun and coworkers investigated VHCF behavior of case carburized CrMn steel by means of the high-frequency fatigue method and found that fatigue crack might initiate either in the carburized case or in the matrix depending on the stress amplitude (Ref 13). Thus, it is necessary to investigate the VHCF properties of case hardening steels for carburized case and for pseudo-carburized core separately.

This work is aimed to compare the VHCF properties of carburized specimens and pseudo-carburized specimens for the case hardening steel DIN 18CrNiMo7-6, which is commonly used for heavy-duty gears due to its good toughness and high fatigue resistance (Ref 13-15). The VHCF characteristics of the experimental steel will be discussed in terms of the microstructure, hardness and nonmetallic inclusions.

Peifeng Cheng, School of Materials Science and Engineering, Kunming University of Science and Technology, Kunming 650093 Yunnan, China; and Institute of Special Steel, Central Iron and Steel Research Institute, Beijing 100081, China; **Yunkun Li**, CN GPower Gearbox Co. Ltd., Chongqing 402263, China; **Wenchao Yu, Jie Shi,** and **Maoqiu Wang**, Institute of Special Steel, Central Iron and Steel Research Institute, Beijing 100081, China; **Shaopeng Yang**, Institute of Special Steel, Central Iron and Steel Research Institute, Beijing 100081, China; and Technology Center, Ma'anshan Iron and Steel Co. Ltd., Ma'anshan 243000 Anhui, China; and **Fangzhong Hu**, Technology Center, Ma'anshan Iron and Steel Co. Ltd., Ma'anshan 243000 Anhui, China; **Li Li**, School of Materials Science and Engineering, Kunming University of Science and Technology, Kunming 650093 Yunnan, China. Contact e-mails: chengpeifeng_1@163.com and maoqiuwang@hotmail.com.

2. Experimental

The material used in this study was 18CrNiMo7-6 gear steel. The chemical compositions (mass percentage) are as follows: 0.17C, 0.26Si, 0.56Mn, 1.70Cr, 1.60Ni, 0.30Mo, 0.01P and 0.005S (Fe balance). All the specimens were machined from 1/2 radius locations of hot-rolled bars with the diameter of 80 mm into the shape of hourglass with a certain amount of finishing margin before heat treatment process. As shown in Fig. 1, some of the specimens were pseudo-carburized at 910 °C for 3 h, and the others were carburized at 910 °C firstly for 14 h at the carbon potential of 1.1% and then for another 14 h at the carbon potential of 0.8%. According to theoretical calculation of carbon diffusion at the carburizing temperature of 910 °C for 28 h, it could result in a carbon content of 0.8% both in the case and in the core. All the carburized specimens and the pseudo-carburized specimens were then tempered at 650 °C for 3 h and air-cooled. After tempering, the specimens were re-austenitized at 860 °C for 1 h, followed by oil quenching and low-temperature tempering at 180 °C for 2 h. After heat treatment, all the specimens were machined into the final dimensions, as shown in Fig. 2.

The microstructure in cross section area of the carburized and pseudo-carburized specimens was observed by means of optical microscopy (OM, Olympus GX51) and scanning electron microscopy (SEM, FEI Quanta 650FEG) after the specimens were cut, polished and etched in 4% nital solution. The distribution of microhardness along the cross section of the specimens was measured by Vickers microhardness tester with a load of 200 g and for a holding time of 15 s. The content of retained austenite in the specimens was calculated according to the measured spectra of XRD on a Brooke D8s type x-ray diffractometer with Co radiation at the target voltage of 35 kV and the current of 40 mA.

To compare the VHCF properties of carburized specimens and pseudo-carburized specimens under axial push–pull loading, fatigue tests with the stress ratio $R = -1$ were carried out on an ultrasonic fatigue testing machine (Shimadzu USF-2000) at the frequency of about 20 kHz. Fatigue tests were performed at room temperature (25 °C) and compressed air was used to reduce the abnormal heat in the middle of the specimen due to
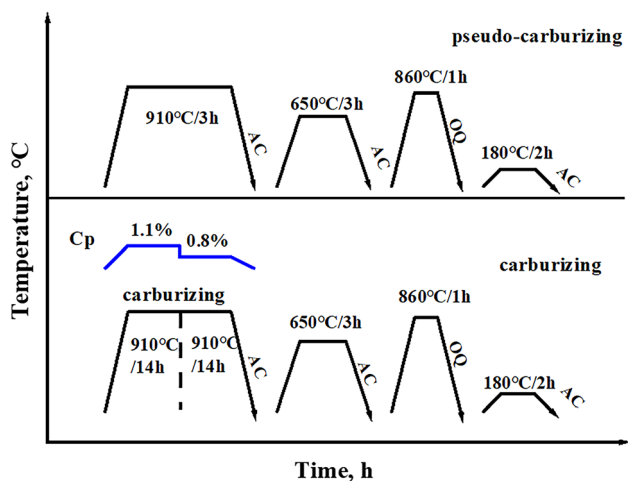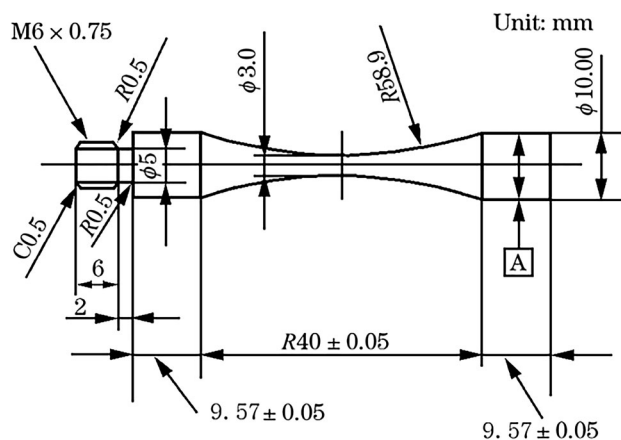
frequency effect. Furthermore, the pulsing and pausing time during cyclic loading was set to 150 ms to further eliminate effect of frequency. Tests were operated till the specimen failure or beyond 10^9 cycles. The fracture surfaces of the failed specimens were observed by means of SEM, and the type of fatigue origin was analyzed by energy-dispersive x-ray spectrometer (EDS). The sizes of nonmetallic inclusions, GBF area and fish-eye area on each fractured specimen were measured according to SEM observations.
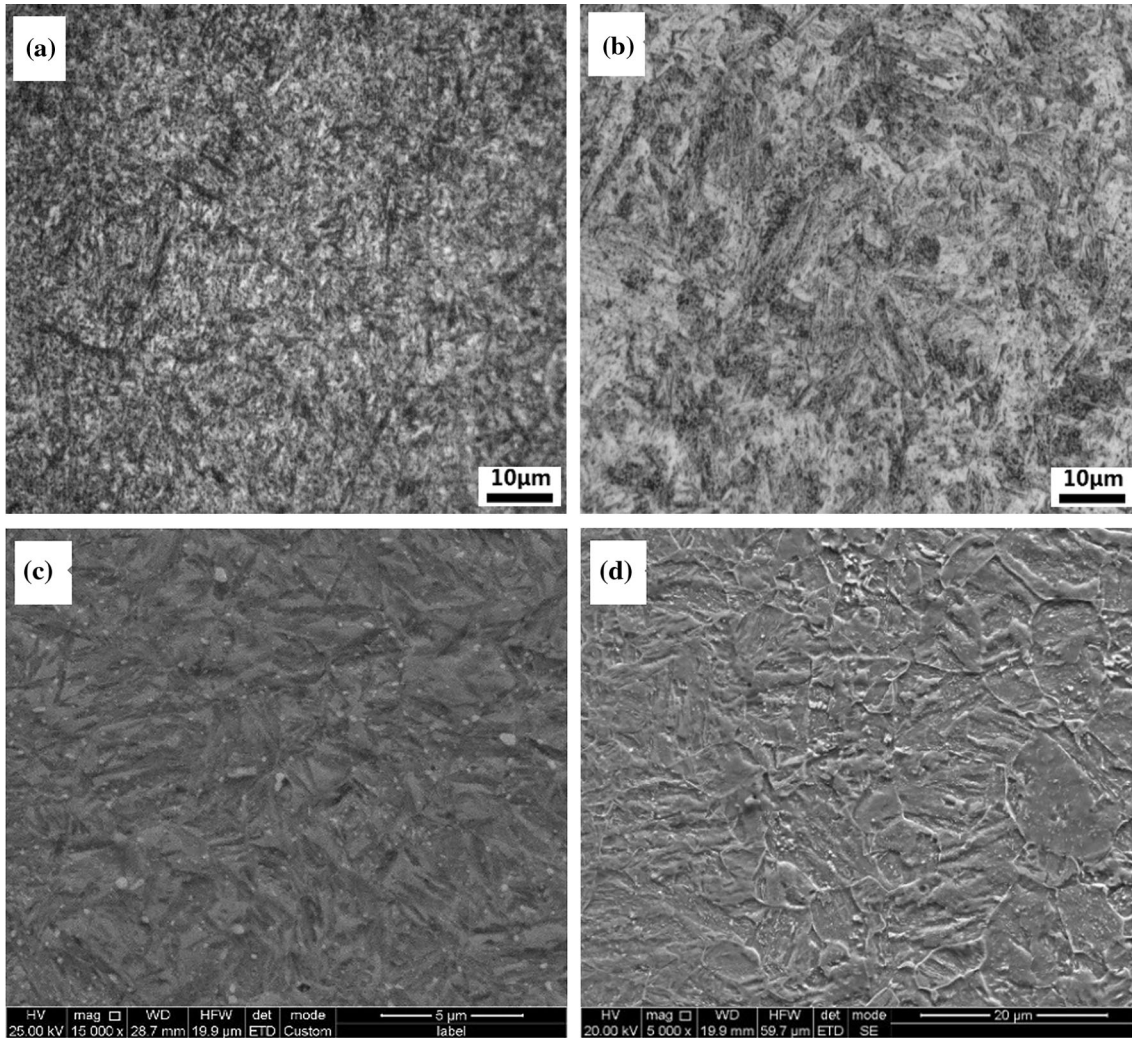
3. Results and Discussion

3.1 Microstructure and Hardness

Figure 3 shows the microstructure of the experimental steel after pseudo-carburized and carburized. For the pseudo-carburized specimen, as shown in Fig. 3(a) and (c), it consisted of lath martensite and carbides, which was presumably precipitated during tempering. For the carburized specimen, it consisted of typical acicular martensite (dark area) and retained austenite (bright area), as shown in Fig. 3(b). Some carbides could be also observed in the microstructure of the carburized specimen, Fig. 3(d). There is no difference in microstructure from the edge area to core area of the carburized specimen. The content of retained austenite was measured by XRD, with the spectra shown in Fig. 4, to be about 20.72% and 0.85% for the carburized and pseudo-carburized specimens, respectively. Carburizing can increase the carbon content remarkably, and it may retard transformation of austenite into martensite during quenching, resulting in a high content of retained austenite in the final microstructure (Ref 10, 16, 17).
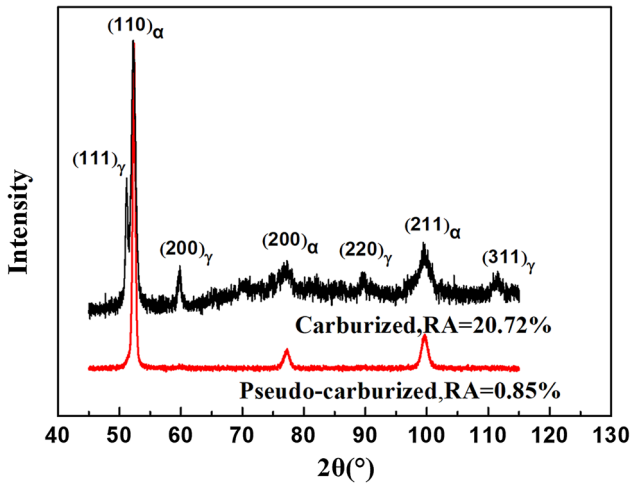
The cross-sectional distribution of microhardness in the pseudo-carburized and carburized specimens is shown in Fig. 5. For both the specimens, the difference in hardness between surface area and core area is ignorable, indicating that the carburized specimen has obtained fully carburized layer through the current carburizing process. The average values were 713 HV and 442 HV for the carburized and pseudo-carburized specimens, respectively. It can be seen that the hardness was remarkably increased by the carburizing treatment.

Fig. 1 Schematic diagram showing the carburizing and heat treatment process, where Cp refers to carbon potential during carburizing
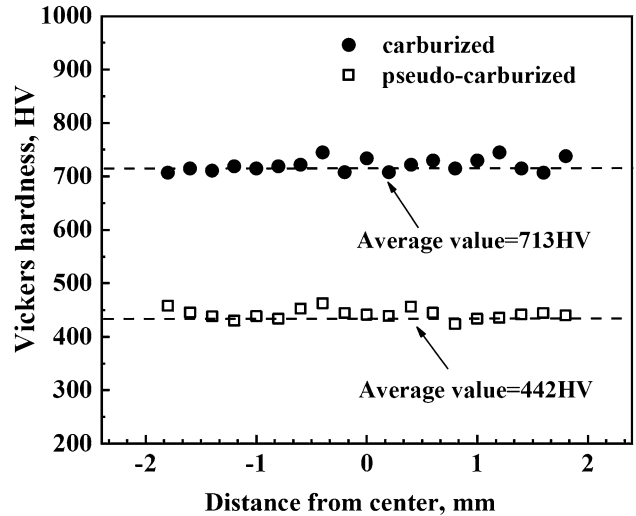

Fig. 2 Shape and dimensions of the specimens used for VHCF tests

Fig. 3 Microstructure of the experimental steel showing (a) and (b) OM images of pseudo-carburized specimen and carburized specimen, and (c) and (d) SEM images of pseudo-carburized specimen and carburized specimen, respectively

Fig. 4 The XRD patterns of carburized and pseudo-carburized specimens

Fig. 5 Cross-sectional distributions of microhardness of the experimental steel
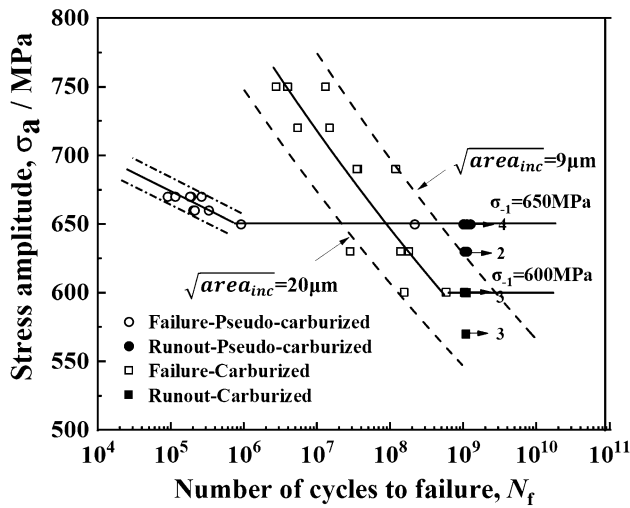
Fig. 6 Fatigue S–N curves of the experimental steel

For the pseudo-carburized specimens, the hardness is mainly dependent on that of the martensite, which is in return on the carbon content of the experimental steel (Ref 18). For the carburized specimens, however, the hardness depends not only on that of the martensite, but also on some other factors such as the content of retained austenite, which is a much softer phase compared with martensite (Ref 19). Under the current heat treatment conditions, the hardness of 713 HV for the carburized specimens and the hardness of 442 HV for the pseudo-carburized specimens are, respectively, consistent with the hardness values in the carburized case and in the core for commonly carburizing treated gears.

3.2 S–N curve

Figure 6 shows the fatigue S–N curves of the experimental steel after carburized and pseudo-carburized. For the pseudo-carburized specimens, as marked by the empty circles in Fig. 6, the number of cycles to failure increased from 10^5 cycles to 10^6 cycles with the decrease in stress amplitude in the range of 700-650 MPa. When the stress amplitude was lower than 650 MPa, the pseudo-carburized specimen did not fracture even after loading for more than 10^9 cycles, as marked by full circles in Fig. 6. Thus, the pseudo-carburized specimen did not show

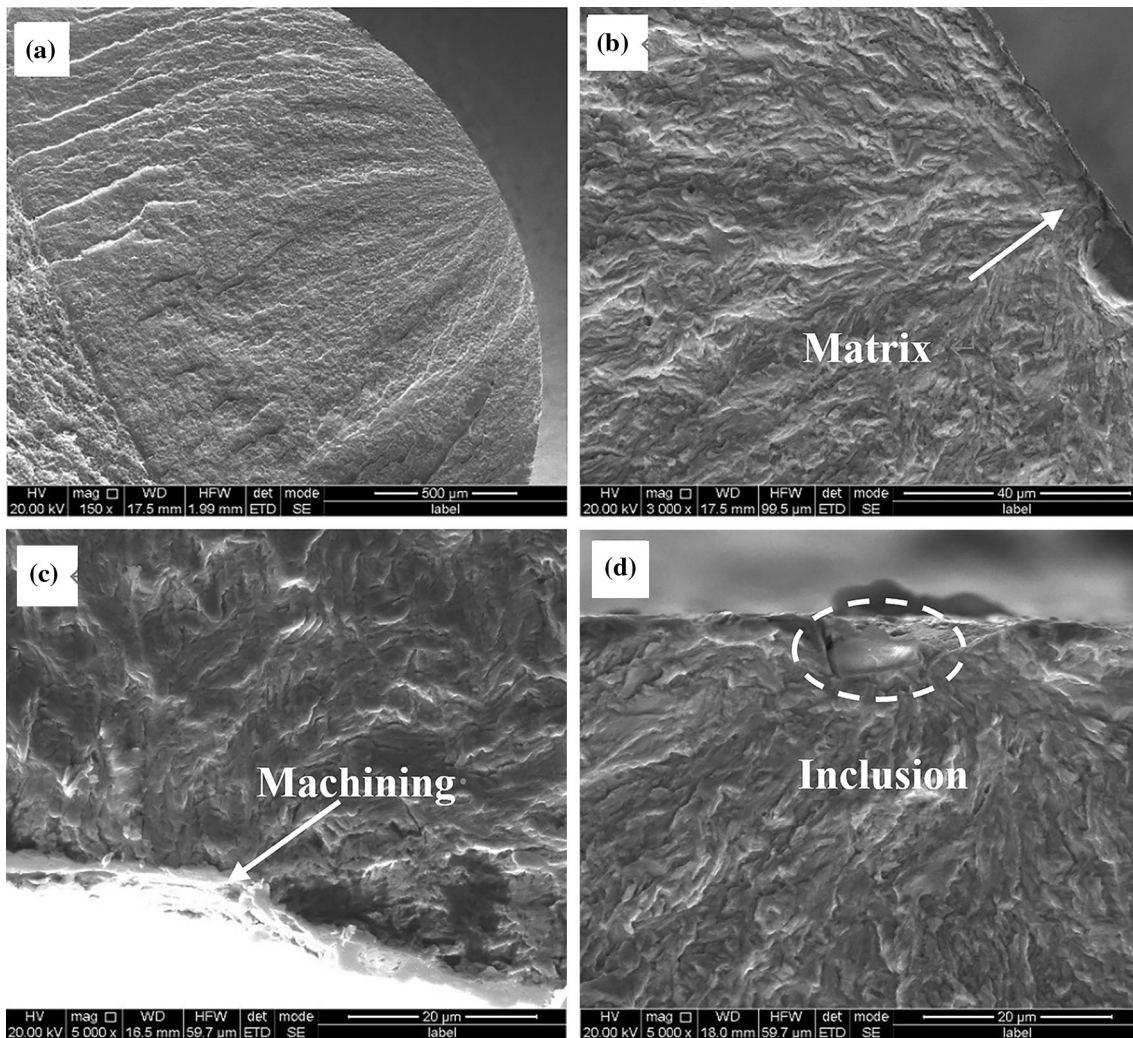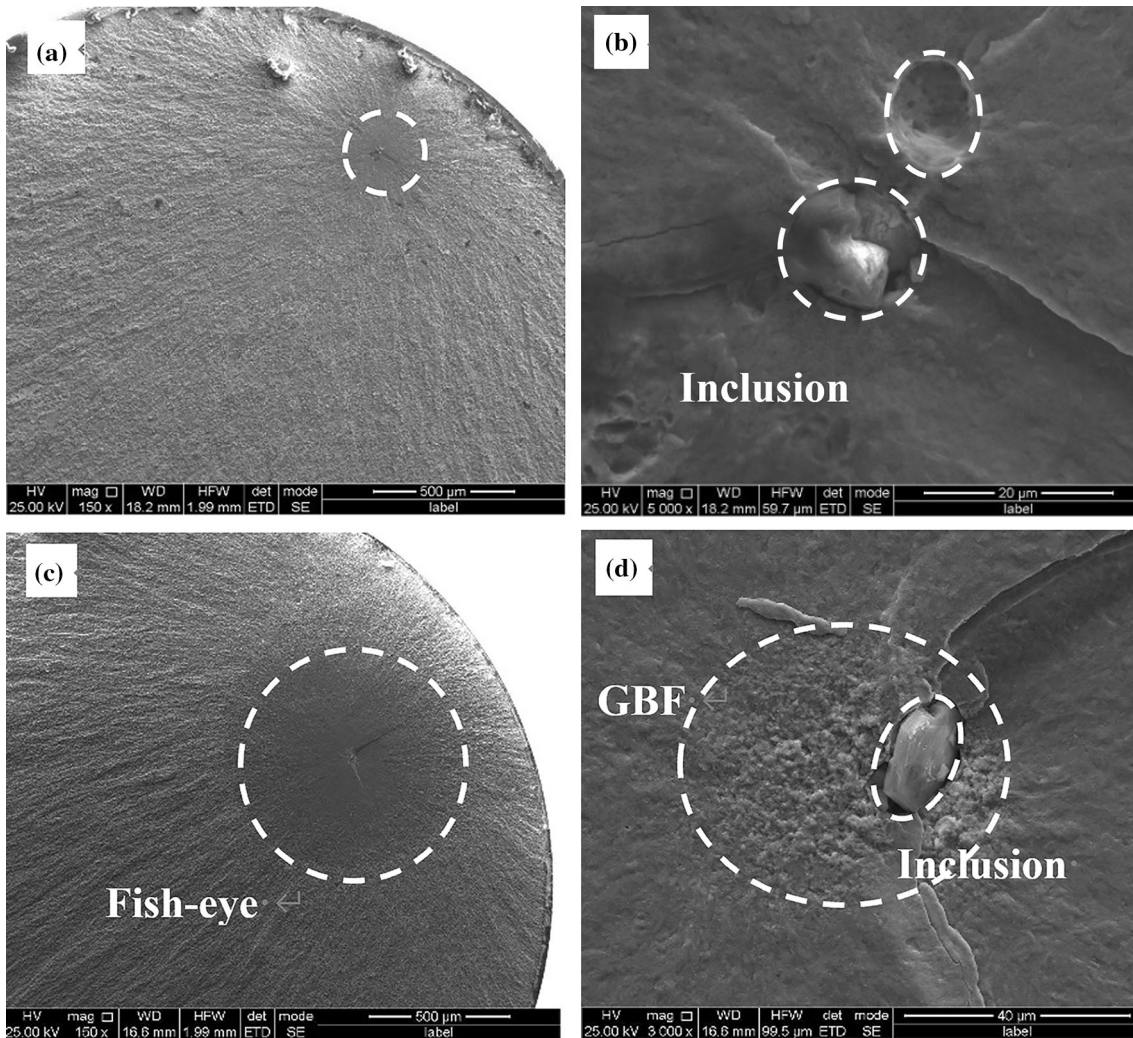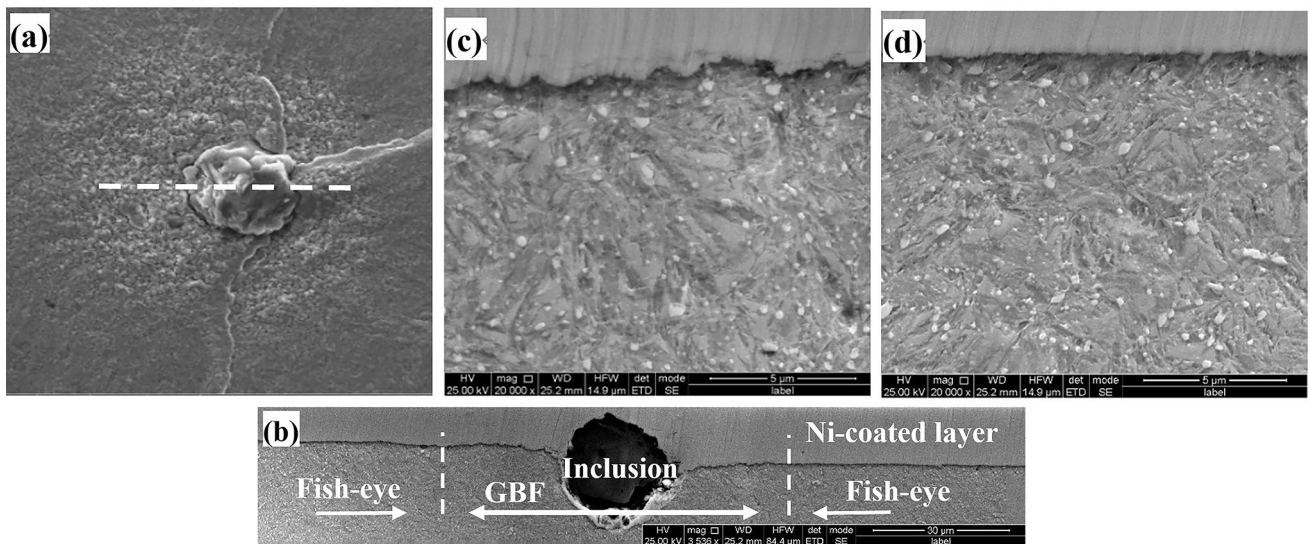
Fig. 7 Fracture surfaces of the fatigue specimens of the experimental steel after pseudo-carburized, (a) and (b) σ_a = 670 MPa, N_f = 2.60E+05, (c) σ_a = 670 MPa, N_f = 8.97E+04 and (d) σ_a = 670 MPa, N_f = 1.88E+05

Fig. 8 Fracture surfaces of the fatigue specimens of the experimental steel after carburized, (a) and (b) $\sigma_a = 800$ MPa, $N_f = 5.54E+05$, and (c) and (d) $\sigma_a = 600$ MPa, $N_f = 1.53E+08$

Fig. 9 SEM micrographs showing cross section of the carburized specimen ($\sigma_a = 680$ MPa, $N_f = 7.50E+08$), (a) and (b) low magnification of fracture surfaces of fish-eye with GBF area, and high magnification of (c) GBF and (d) fish-eye area

Table 1 Fatigue crack origins measured from fracture surfaces

No.	Stress, MPa	N_f, cycle	$\sqrt{area_{inc}}$, µm	$\sqrt{area_{GBF}}$, µm	$\sqrt{area_{FiE}}$, µm	Depth, µm
1	600	1.02E+09	12.28	39.03	269.22	104.90
2	600	5.77E+08	13.53	39.44	480.76	335.22
3	600	1.53E+08	15.33	49.58	463.93	592.30
4	630	1.37E+08	19.93	39.96	308.87	1000.31
5	630	2.79E+07	15.33	38.64	472.30	461.00
6	630	1.78E+08	17.24	43.52	456.40	373.43
7	630	1.16E+07	10.04	36.83	258.97	1061.78
8	690	3.56E+07	12.23	29.94	221.18	169.92
9	690	1.17E+08	10.06	33.39	490.88	361.20
10	690	3.42E+07	11.29	30.75	373.71	798.11
11	720	5.32E+06	12.23	28.79	392.44	258.35
12	720	1.45E+07	14.35	25.62	181.71	82.23
13	750	2.70E+06	15.45	24.67	324.40	150.03
14	750	1.28E+07	15.53	39.82	308.89	1031.04
15	750	3.86E+06	17.41	23.47	465.98	332.02
16	770	3.33E+07	9.04	29.72	178.29	77.32
17	800	5.54E+05	15.78	–	256.91	383.36
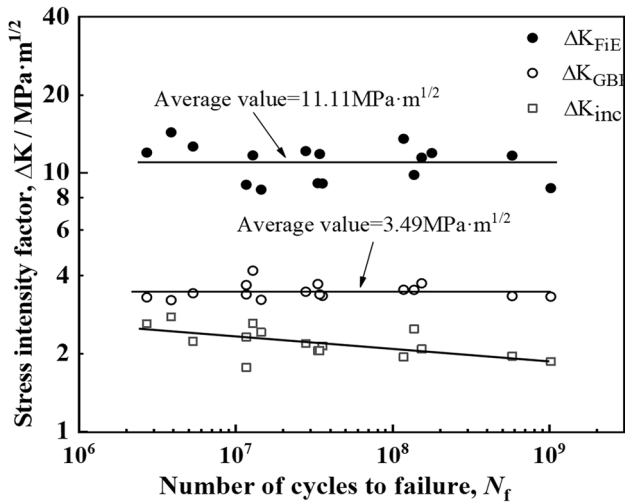
Fig. 10 The relationship between ΔK_{inc}, ΔK_{GBF}, ΔK_{FiE} and fatigue life for the carburized specimens of the experimental steel

VHCF behavior and the fatigue limit at 10^9 cycles could be regarded to be 650 MPa, which was also the fatigue limit at 10^7 cycles.

For the carburized specimens, as marked by the rectangular symbols in Fig. 6, the number of cycles to failure increased from 10^6 cycles to 10^9 cycles with the decrease in stress amplitude in the range of 750-600 MPa. According to the test results, the number of cycles to failure was more than 10^7 cycles when the stress amplitude was lower than 700 MPa. When the stress amplitude was lower than 600 MPa, the carburized specimen did not fracture even after loading for more than 10^9 cycles. Thus, the carburized specimen showed VHCF behavior, and the fatigue limit at 10^9 cycles was measured to be 600 MPa.

Some scatters of the data points in Fig. 6 could be seen especially for the carburized specimens in the very high cycle regime, presumably due to the relatively large scatter in the case hardness. Several models have been proposed for description of VHCF S–N curves of high-strength steels (Ref 20-22).

Recently, Furuya revised Tanaka-Akimina's model and proposed a new prediction model of ultra-high cycle fatigue strength (Ref 22). The solid line near the carburizing pattern in Fig. 6 was fitted according to this new model. In this fitting, the R^2 value (determination coefficient) reflecting the goodness of fit is 0.7871. According to these results, the fatigue life curves (dashed lines) of the minimum inclusion size of $\sqrt{area_{inc}} = 9$ µm and the maximum inclusion size $\sqrt{area_{inc}} = 20$ µm were predicted, and it could be seen that the measured points were basically between these two curves. The related formulae of the model are as follows,

$$\frac{d\sqrt{area}}{dN} = C\left(\Delta K \cdot \sqrt{area}^{\alpha}\right)^m \tag{Eq 1}$$

$$\sigma_a = \frac{1}{\sqrt{\pi}}(D)^{\frac{1}{m}} \times (N_f)^{-\frac{1}{m}} \times \left(\sqrt{area_{inc}}\right)^{\left(\frac{1}{m}-\frac{1}{2}-\alpha\right)} \tag{Eq 2}$$

$$\left(\Delta K_{inc} \cdot \sqrt{area_{inc}}^{\alpha}\right)^m \left(\frac{N_f}{\sqrt{area_{inc}}}\right) = \frac{2^{1-m\left(\frac{1}{2}+\alpha\right)}-1}{C\left(1-m\left(\frac{1}{2}+\alpha\right)\right)} = D \tag{Eq 3}$$

where m, D and α are constants that determine the crack propagation properties. D is a constant that simplifies the right side of Eq 3. Through the nonlinear fitting, we can obtain the parameters for the carburized specimens of the experimental steel as follows, $D = 5.24 \times 10^{56}$, $m = 22.03$, $\alpha = -0.28$, $R^2 = 0.7871$. The fatigue lives of the carburized specimen of the experimental steel in the very high cycle regime could be predicted by using the above equations, indicating that the VHCF properties of carburized gear steels should be similar to those of bearing steels, which were extensively investigated.

3.3 Fractography

Under axial push–pull cyclic loading, the failure mode of the pseudo-carburized specimens was mainly surface initiated, and the types of crack origin could be categorized into inhomogeneous matrix, defects by machining process, and surface inclusions based on the observations of fracture

Table 2   Comparison of VHCF limits and ΔK_{GBF} values of high-strength steels

Steel	σ_{-1}, MPa	Hardness, HV	$\sqrt{area_{Inc}}$, μm	$\sqrt{area_{GBF}}$, μm	ΔK_{GBF}	Reference
18CrNiMo7-6 (carburized)	650	719	13.9	32.5	3.49	Present
US150	840	820	17.0	23.8-37.4	4-6	Ref 21
SNCM439	925	586	14.7	22.05-44.1	4	Ref 24
SUJ2	765	807	19.2	47.1	4.65	Ref 25

surfaces, as shown in Fig. 7. Pseudo-carburized specimens did not show VHCF failure and the features of VHCF failure such as interior inclusion initiated GBF area and fish-eye area were not observed.

Different from the surface failure mode of pseudo-carburized specimens, interior failure mode occurred in the carburized specimens. Typical fracture surface with interior failure of the carburized specimens is shown in Fig. 8. The fish-eye feature on the surface of fatigue fracture is obvious, as shown in Fig. 8(a) and (c). The fracture surface of the specimen with 800 MPa stress loading did not have GBF feature around the inclusion (Fig. 8b), but GBF area could be clearly seen on the fracture surface of the specimen with 600 MPa stress loading (Fig. 8d). Meanwhile, the fatigue life of the specimen without GBF and the one with GBF was 5.54×10^5 cycles and 1.53×10^8 cycles, respectively, indicating that GBF might play a significant role in VHCF regime.

Figure 9 shows the cross section around the inclusion and GBF area for a carburized specimen, which was fractured after more than 10^8 cycles under the stress amplitude of 680 MPa. It can be seen that the fracture surface in the GBF area was much rougher in comparison with that in the other fish-eye area, as shown in Fig. 9(c) and (d). The roughness of the fracture surface in the GBF area was estimated to be 0.23 μm, with the maximum value of 0.93 μm (Ref 23). It was regarded to be formed due to numbers of cyclic loading and the measured results were in agreement with those for SNCM 439 steel reported by Shiozawa (Ref 24).

3.4 Stress Intensity Factor

The data of fatigue test results and the measurement results of dimensions related to inclusion, GBF area and fish-eye area on fracture surfaces are listed in Table 1, and the sizes of inclusion, GBF area and fish-eye area are represented by $\sqrt{area_{inc}}$, $\sqrt{area_{GBF}}$ and $\sqrt{area_{FiE}}$, respectively. It can be seen that the fatigue life increased with the decrease in stress amplitude, but it is hard to find the relation between $\sqrt{area_{inc}}$, $\sqrt{area_{GBF}}$ or $\sqrt{area_{FiE}}$ and fatigue life of specimens directly. It can be also seen that the inclusion size $\sqrt{area_{inc}}$ was in the range of 9 to 20 μm, and the average value was about 14 μm. The size of GBF area $\sqrt{area_{GBF}}$ was ranged from 23 to 50 μm with the average value of about 35 μm. The mean size of fish-eye area $\sqrt{area_{FiE}}$ was measured to be about 347 μm with a range from 178 to 490 μm. It is also noted that the depth of crack initiation site was ranged from 77 to 1062 μm.

For the purpose of investigating the effect of $\sqrt{area_{inc}}$, $\sqrt{area_{GBF}}$ and $\sqrt{area_{FiE}}$ on fatigue life and fatigue strength, the stress intensity range ΔK was calculated by using the formula as follows,

$$\Delta K = 0.5 \Delta\sigma \sqrt{\pi\sqrt{area}}, \quad \Delta\sigma = 2\sigma_a \qquad \text{(Eq 4)}$$

where $\sqrt{area}$ is a crack size defined as the square root of measurement area, and σ_a is the stress amplitude. Figure 10 shows the plot of the calculation data ΔK and fatigue life N_f. It can be seen that the value of ΔK_{GBF} and ΔK_{FiE} did not change with the increase of N_f but fluctuated within a narrow range. Thus, the values of ΔK_{GBF} and ΔK_{FiE} could be regarded as constant, with the average values being 3.49 and 11.11 MPa·m$^{1/2}$, respectively, for the carburized specimens of the experiment steel. ΔK_{GBF} could be regarded as the threshold value of crack initiation ΔK_{th}, which means that fatigue short-crack would not propagate and form a fish-eye when the stress intensity factor at crack edge $\Delta K < \Delta K_{th}$. Similarly, ΔK_{FiE} also could be regarded as the critical value of crack propagation, and when $\Delta K < \Delta K_{FiE}$, the fatigue long-crack could not propagate and cause final abrupt fracture. It can be seen that the value of ΔK_{Inc} decreased with the increase of N_f.

Table 2 lists the results of VHCF limits and ΔK_{GBF} values of some high-strength steels (Ref 21, 24, 25). The VHCF limit of the carburized specimens of the experimental steel was lower than those of bearing steel SUJ2, spring steel US150 and SNCM439, with different hardness. The ΔK_{GBF} of the experimental steel was also the lowest among the listed steels. As can be seen in Table 2, the sizes of inclusions and GBF area of the steels are comparable, indicating that VHCF crack initiation might be in a similar way. However, the VHCF properties of the steels are quite different. It is not only dependent on the hardness, but also on the microstructural characteristics. Since retained austenite is a much softer phase compared with martensite, the high value of retained austenite in the carburized case of the experimental steel could be related to its low VHCF limit and ΔK_{GBF}. Thus, further work is still needed concerning the role of retained austenite so as to clarify the mechanisms of VHCF behavior of the experimental steel.

4. Conclusions

In this work, VHCF properties of DIN 18CrNiMo7-6 gear steel after pseudo-carburizing and carburizing were investigated by means of ultrasonic fatigue tests. The fracture surfaces of the fatigue specimens were observed on SEM. The following conclusions can be drawn.

1. The pseudo-carburized specimens of the experimental steel did not show VHCF behavior, and the high cycle fatigue limit of 650 MPa at 10^7 cycles could be also regarded as the VHCF fatigue limit.
2. The carburized specimens of the experimental steel showed typical VHCF behavior, and the fatigue limit at 10^9 cycle was measured to be 600 MPa. The VHCF S–N curve could be predicted by a theoretical model taking into account of nonmetallic inclusion sizes.

3. For the carburized specimens of the experimental steel, the stress intensity factor value ΔK_{GBF} at GBF area was measured to be around 3.5 MPa m$^{-1/2}$, and it was lower than those of high-strength steels, which could presumably be related to the high content of retained austenite in the carburized layer.

Conflict of interest

The authors declare no conflict of interest.

References

1. T. Sakai, B. Lian, M. Takeda, K. Shiozawa, N. Oguma, Y. Ochi, M. Nakajima, and T. Nakamura, Statistical Duplex S–N Characteristics of High Carbon Chromium Bearing Steel in Rotating Bending in Very High Cycle Regime, *Int. J. Fatigue*, 2010, **32**, p 497–504
2. W. Li, T. Sakai, M. Wakita, and S. Mimura, Influence of Microstructure and Surface Defect on Very High Cycle Fatigue Properties of Clean Spring Steel, *Int. J. Fatigue*, 2014, **60**, p 48–56
3. Y. Furuya, Gigacycle Fatigue Properties of Double-Melted SCM440 Steel and Size Effects, *ISIJ Int.*, 2014, **52**, p 1436–1442
4. Z.G. Yang, S.X. Li, J.M. Zhang, J.F. Zhang, G.Y. Li, Z.B. Li, W.J. Hui, and Y.Q. Weng, The Fatigue Behaviors of Zero-Inclusion and Commercial 42CrMo Steels in the Super-Long Fatigue Life Regime, *Acta Mater.*, 2004, **52**, p 5235–5241
5. Y. Murakami, *Metal Fatigue: Effect of Small Defects and Nonmetallic Inclusions*, Elsevier, Oxford, 2002
6. T.D. Jeddi and T. Palin-Luc, A Review about the Effects of Structural and Operational Factors on the Gigacycle Fatigue of Steels, *Fatigue Fract. Eng. Mater. Struct.*, 2018, **41**, p 969–990
7. Y. Murakami, T. Nomoto, and T. Ueda, On the Mechanism of Fatigue Failure in the Superlong Life Regime (N > 107 Cycles). Part 1: Influence of Hydrogen Trapped by Inclusions, *Fatigue Fract. Eng. Mater. Struct.*, 2010, **23**, p 893–902
8. T. Naito, H. Ueda, and M. Kikuchi, Fatigue Behavior of Carburized Steel with Internal Oxides and Nonmartensitic Microstructure near the Surface, *Metall. Mater. Trans. A*, 1984, **15A**, p 1431–1436
9. A. Nehila, W. Li, N. Gao, X. Xing, H. Zhao, P. Wang, and T. Sakai, Very High Cycle Fatigue of Surface Carburized CrNi Steel at Variable Stress Ratio: Failure Analysis and Life Prediction, *Int. J. Fatigue*, 2018, **111**, p 112–123
10. G. Krauss, The Microstructure and Fracture of a Carburized Steel, *Metall. Mater. Trans. A*, 1978, **9**, p 1527–1535
11. M. Erdogan and S. Tekeli, The Effect of Martensite Volume Fraction and Particle Size on the Tensile Properties of a Surface-Carburized AISI 8620 Steel with a Dual-Phase Core Microstructure, *Mater. Charact.*, 2003, **49**, p 445–454
12. Y. Liu, M.Q. Wang, J. Shi, W.J. Hui, G. Fan, and H. Dong, Fatigue Properties of Two Case Hardening Steels after Carburization, *Int. J. Fatigue*, 2009, **31**, p 292–299
13. C.F. Wang, M.Q. Wang, J. Shi, W.J. Hui, and H. Dong, Effect of Microstructural Refinement on the Toughness of Low Carbon Martensitic Steel, *Scr. Mater.*, 2008, **58**, p 492–495
14. W. Chen, X.F. He, W.C. Yu, J. Shi, M.Q. Wang, and K.F. Yao, Nano- and Microhardness Distribution in the Carburized Case of Nb-Microalloyed Gear Steel, *J. Mater. Eng. Perform.*, 2020, https://doi.org/10.1007/s1165-020-04992-7
15. S. Huang, G.Q. Zhang, M.Q. Wang, and H.L. Tan, Fatigue Properties of Heavy-Duty Gear Steel with Different Case Depth, *J. Iron. Steel Res. Int.*, 2012, **24**, p 34–48
16. G. Parrish, Carburizing: Microstructures and Properties, *Heat Treat. Met.*, 1999, **27**, p 2
17. S. Roy and S. Sundararajan, The Effect of Heat Treatment Routes on the Retained Austenite and Tribomechanical Properties of Carburized AISI 8620 Steel, *Surf. Coat. Technol.*, 2016, **308**, p 236–243
18. E.C. Henry, C. O'Brien, and H.K. Yeddu, Multi-length Scale Modeling of Carburization, Martensitic Microstructure Evolution and Fatigue Properties of Steel Gears, *J. Mater. Sci. Technol.*, 2020, **49**, p 157–165
19. B. Wang, Y.Q. He, Y. Liu, Y. Tian, J.L. You, Z.D. Wang, and G.D. Wang, Materials, Mechanism of the Microstructural Evolution of 18Cr2Ni4WA Steel during Vacuum Low-Pressure Carburizing Heat Treatment and Its Effect on Case Hardness, *Materials*, 2020, **13**, p 2352–2368. https://doi.org/10.3390/mal13102352
20. T. Sakai, N. Oguma, and A. Morikawa, Microscopic and Nanoscopic Observations of Metallurgical Structures Around Inclusions at Interior Crack Initiation Site for a Bearing Steel in Very High-Cycle Fatigue, *Fatigue Fract. Eng. Mater. Struct.*, 2015, **38**, p 1305–1314
21. Z.Q. Lei, Y.S. Hong, J. Xie, C.Q. Sun, and A.G. Zhao, Effects of Inclusion Size and Location on Very-High-Cycle Fatigue Behavior for High Strength Steels, *J. Mater. Sci. Eng. A*, 2012, **558**, p 234–241
22. Y. Furuya, A New Model for Predicting the Gigacycle Fatigue Strength of High-Strength, *J. Mater. Sci. Eng*, 2019, **743**, p 445–452
23. K. Shiozawa, Y. Morii, S. Nishino, and L. Lu, Subsurface Crack Initiation and Propagation Mechanism in High-Strength Steel in a Very High Cycle Fatigue Regime, *Int. J. Fatigue*, 2006, **28**, p 1521–1532
24. K. Shiozawa, M. Murai, Y. Shimatani, and T. Yoshimoto, Transition of Fatigue Failure Mode of Ni-Cr-Mo Low-Alloy Steel in Very High Cycle Regime, *Int. J. Fatigue*, 2010, **32**, p 541–550
25. Y.D. Li, N. Xu, H. Ma, and Y.Z. Li, Granular Bright Fact Crack Propagating under Very High Cycle Fatigue, *Mater. Sci. Technol.*, 2016, **31**, p 1894–1902